Tellus SERIES A DYNAMIC METEOROLOGY AND OCEANOGRAPHY
PUBLISHED BY THE INTERNATIONAL METEOROLOGICAL INSTITUTE IN STOCKHOLM

Tellus (2008), 60A, 775–788
Printed in Singapore. All rights reserved

TELLUS

Modelling of warm-air advection over Arctic sea ice

By PRIIT TISLER[1*], TIMO VIHMA[1], GERD MÜLLER[2] and BURGHARD BRÜMMER[2],
[1]*Meteorological Research, Finnish Meteorological Institute, Erik Palménin aukio 1, P.O.Box 503, FI-00101 Helsinki, Finland;* [2]*Meteorological Institute, University of Hamburg, Bundesstrasse 55, D-20146 Hamburg, Germany*

(Manuscript received 25 September 2007; in final form 7 January 2008)

ABSTRACT

The evolution of the atmospheric boundary layer (ABL) during warm-air advection over sea ice in the Fram Strait is investigated. A hierarchy of numerical models is applied and the results are validated against aircraft observations. Operational HIRLAM (HIgh Resolution Limited Area Model) runs suffered from inaccurate information on the location of the sea ice edge. When this was improved, together with improving the horizontal resolution, the HIRLAM results became much better. Two-dimensional model runs with inflow boundary conditions prescribed according to the aircraft observations demonstrated that the contribution of thin ice (re-frozen leads) is important. The modelled turbulent fluxes of momentum, sensible heat and latent heat showed a large vertical divergence from the surface to the height of the aircraft observations. Above a 4-km-wide open lead, the modelled heat fluxes at the observation height of 24 m agreed reasonably well with the observations but were on average only 6% (sensible heat) and 13% (latent heat) of the modelled surface values. Model experiments showed that in this case relatively high values for the roughness length z_0 over sea ice yielded better agreement with the observed wind speed than values commonly used in numerical models.

1. Introduction

Warm-air advection is highly important for the climate in the Polar regions. Together with cloud-radiative forcing and wind-generated turbulent mixing, it is the main factor controlling the boundary-layer air and snow surface temperature in winter (Vihma and Pirazzini, 2005). It has a large effect on the onset of snow melt in spring, and due to the albedo feedback it further affects the snow and sea ice mass balance. Since 1990s, large positive anomalies have been observed in the near-surface air temperature in the Arctic, and they have been strongly associated with patterns of warm-air advection (Overland et al., 2004). Modelling of the Polar atmosphere is sensitive to the information of sea ice concentration (SIC) both in cases of cold-air outbreaks (Valkonen et al., 2008) and warm-air advection (Maslanik et al., 2000). Also, the most extreme temperature inversions in the Arctic, which pose a problem for numerical models, are often related to warm-air advection (Bradley et al., 1992). Processes in the atmospheric boundary layer (ABL) during warm-air advection over the Arctic sea ice have, however, not been studied much.

Over the marginal sea ice zone, the ABL is usually not in balance with the local surface. While crossing the ice edge the flow has to adjust to changed conditions with respect to surface roughness and temperature: the air mass is modified and an internal boundary layer (IBL) develops. The ABL modification is very different between cases of an on-ice and off-ice air flow. During off-ice flow (Brümmer, 1996; Olsson and Harrington, 2000; Inoue et al., 2005), a cold and dry air mass is advected over the open ocean resulting in strong convection and often in cloud formation. Because of the unstable stratification, the surface fluxes are large and the IBL grows rapidly. The sea surface temperature is only slightly affected by the cold air mass. On the contrary, during warm-air advection over sea ice, that is on-ice flow, there is a strong coupling between the air temperature and the surface temperature of the sea ice. This is due to the low thermal conductivity of ice and especially of snow. During an on-ice flow, a shallow stable IBL develops over the ice, and the surface fluxes downwind of the ice edge tend to be much smaller than during off-ice flow. Typically, on-ice flow brings along warm and moist air, resulting quite frequently in formation of low clouds and fog. The ice edge is compact due to on-ice wind packing the ice. On the contrary, off-ice winds lead to a wide zone with inhomogeneous and fractional sea ice cover, characterised by floes of various size.

Most of the previous studies on warm-air advection over sea ice have been based on aircraft or ship observations or numerical modelling, but seldom on both. The first studies were based on rawinsonde sounding data from a moving ship in the Antarctic sea ice zone (Andreas et al., 1984) and aircraft observations from the Fram Strait (Fairall and Markson, 1987; Brümmer et al., 1994). Guest et al. (1995) presented a review with a focus on wind

*Corresponding author.
e-mail: priit.tisler@fmi.fi
DOI: 10.1111/j.1600-0870.2008.00316.x

and momentum flux fields in various flow conditions. Brümmer et al. (2002) and Vihma and Brümmer (2002) analysed aircraft observations over the Baltic Sea. In a number of study cases of warm-air advection over sea ice, the air mass modification has been relatively small. In Vihma and Brümmer (2002), the ABL cooling was of the order of 1 K. In Brümmer et al. (1994), in late spring, the cooling was only a few tenths of a Kelvin over horizontal distances of 100–300 km. In Brümmer and Thiemann (2002), in early spring, however, a strong cooling was observed over a 300-km-long flight track over sea ice northwest of Svalbard.

The first modelling study on warm-air advection over sea ice was presented by Bennett and Hunkins (1986), based on data of Andreas et al. (1984). The two-dimensional modelling focused on the contributions of surface heat fluxes, radiative flux divergence, and adiabatic cooling to the air-mass cooling. Kantha and Mellor (1989) made idealized two-dimensional simulations of warm-air advection over sea ice but no comparisons with observations. The modelling study of Glendening (1994) addressed various flow conditions over the ice edge zone, but without detailed validation. Also, the coupled modelling of ABL and sea ice thermodynamics during warm-air advection by Cheng and Vihma (2002) was idealized without validation. Vihma et al. (2003) presented the first combination of detailed observations (including spatial distribution of turbulent fluxes) and modelling of a significant air-mass modification during an on-ice air flow.

The objective of our paper is to better understand the problems in modelling of warm-air advection over sea ice. The aircraft observations of Brümmer and Thiemann (2002) are applied for validation of the model experiments (Section 2). We selected these observations, because the case was particularly interesting: the flight track over sea ice was longer than in other previous studies, and the observations on the ABL included three clearly different stages: development of a shallow stably stratified boundary layer, its deepening due to cloud radiative forcing, and crossing of a synoptic-scale front. We address this case by a hierarchy of model experiments (Section 3). First, results of three-dimensional mesoscale model HIRLAM are examined and compared with observations (Section 4). Experiments are carried out initially at coarse-resolution operational mode and later with increased horizontal resolution and improved SIC. Second, we perform a number of sensitivity tests making use of a two-dimensional model, employing very high horizontal and vertical resolution. Here, the inflow boundary conditions as well as sea ice type and roughness can be prescribed according to observations allowing us to distinguish between error sources related to initial/boundary conditions and modelling/parameterization of physical processes (Section 5).

2. Observational data

Observational data used in this study were gathered by an aircraft campaign, conducted in March 1998 over the Fram Strait region between Spitsbergen and Greenland (Brümmer and Thiemann, 1999; 2002). This aircraft experiment was part of a German research contribution to the Arctic Climate System Study (ACSYS). The objective of this project was to experimentally investigate the air-mass modification in on-ice air flow and the physical processes involved there. Systematic measurements were performed on 12 March over a distance of 300 km, resulting in a unique dataset. Air-mass modification and boundary-layer evolution was observed starting over the open sea. After passing the ice edge, a transition from unstable stratification over the open sea to stable stratification over the ice began, resulting in development of a shallow stably stratified IBL.

The flight pattern consisted of a downwind cross-section from southeast to northwest with a sequence of low-level horizontal flight legs and vertical profiles. To evaluate our model results in detail, a notable set of in situ measured meteorological quantities was utilized. Measurements on air temperature, wind speed and direction, water vapour mixing ratio, shortwave and longwave radiation, as well as turbulent fluxes of momentum, sensible heat and latent heat at an average height of 24 m along the 300-km-long flight leg were used. In addition, three selected aircraft vertical profiles of wind, temperature and humidity were applied for model validation, representing (a) initial conditions of the air flow over the open water (profile P01 at $x = -36$ km, where x is the distance downwind of the ice edge), (b) development of a shallow stable IBL over the ice in cloudless conditions (profile P07; $x = 101$ km) and (c) radiation effect of clouds on the boundary layer structure (profile P12; $x = 258$ km). For details on the measurements and data analyses, see Brümmer and Thiemann (2002).

3. Models and experiments

The modelling strategy is presented in Table 1. The purpose of HIRLAM experiment H1 is to understand the problems present in operational modelling over the Arctic sea ice. Experiment H2 is made to eliminate errors due to inaccurate ice concentration, and to study the effects of improved resolution. When a large number of experiments are needed, the 2D model is more practical. The 2D experiments, identified as 2D1–2D7, are made to eliminate errors due to inaccurate inflow boundary conditions, and to make sensitivity tests with respect to ice surface roughness z_0, ice thickness distribution, and stability effects on turbulence.

3.1. HIRLAM

3.1.1. Model description. The HIRLAM model is used as the basis for operational short-range weather prediction at several European national meteorological services. HIRLAM is a hydrostatic limited-area grid-point model with lateral boundary values given by a large-scale model, for example that of the European Centre for Medium-Range Weather Forecasts (ECMWF).

Table 1. Model experiments

Experiment	Description
H1	HIRLAM, 22 km horizontal resolution, boundaries and sea ice concentration from ECMWF, $z_0 = 3$ cm over sea ice
H2	HIRLAM, 9 km horizontal resolution, boundaries from H1, corrected sea ice concentration, $z_0 = 3$ cm
H3	As H2, but $z_0 = 3$ mm
2D1	Surface temperature (T_S) prescribed, $z_0 = 1$ cm
2D2	T_S modelled, $z_0 = 1$ cm
2D3	T_S modelled but without thin ice, $z_0 = 1$ cm
2D4	T_S modelled, $z_0 = 1$ mm
2D5	T_S modelled, z_0 based on equations (3) to (5)
2D6	T_S prescribed, $z_0 = 1$ cm, larger background turbulence: b = 0.1 in eq. (2)
2D7	T_S prescribed, $z_0 = 1$ cm, stability dependence of turbulent surface fluxes as in HIRLAM

HIRLAM is based on the primitive equations; the dependent variables are temperature, wind components, humidity, surface pressure, cloud water content and turbulent kinetic energy (Källen, 1996; Undén et al., 2002). In the current study, the HIRLAM reference version 6.4.3 (Cats, 2005) was used. The HIRLAM radiation scheme is based on Savijärvi (1990) and also documented in Sass et al. (1994). It is fairly simple and computationally efficient, but nevertheless reasonably accurate (Niemelä et al., 2001a, b; van Mejgaard et al., 2001). The turbulence scheme is based on prognostic turbulent kinetic energy, the so-called CBR scheme (Cuxart et al., 2000). In addition, an improved formulation for the mixing length scale (Lenderink and De Rooy, 2000) and the rotation of the stress vector (Tijm, 2004) are adopted. This in turn leads to more realistic wind profile predictions in the lowest atmosphere.

Turbulent surface fluxes are computed according to the Monin-Obukhov similarity theory, which takes into account surface roughness and the stability of the surface layer. The surface parameterization is based on mosaic approach (aggregation of fluxes); five different surface tiles are allowed within each grid square: water, ice, bare ground, low vegetation and forest. For this study, the most essential surface types are sea ice and open sea. In order to obtain the SIC in HIRLAM no analysis is performed, that is neither ECMWF pseudo observations nor satellite measurements of the ice cover are used. Instead, the SIC is diagnosed linearly from the sea surface temperature (SST), assuming that SIC reaches 100% at -1.7 °C and 0% when SST > 0 °C (Homleid et al., 2005). SST in turn is analysed/updated making use of the successive correction method, by using the previous analysis as the background field, relaxed to its climatological value. Data used are observations contained in sea surface reports (SHIP and BUOY) and pseudo observations created from the ECMWF SST, which is based on the daily National Centre of Environmental Prediction (NCEP) global SST analysis (Undén et al., 2002). When the SIC is determined, the ice surface temperature is calculated at each time-step applying the force-restore method, which takes into account the conductive heat flux through the ice.

Diagnostic fields, such as 2 m temperature and relative humidity and 10 m wind are computed and are available for each grid box fraction separately. The time-integration is performed by semi-lagrangian advection scheme and the analysis system uses variational data assimilation (3D-Var) technique.

3.1.2. Experiment setup. For the present experiments, two different grids were applied. First, we exploited the main operational suite of HIRLAM, as applied at Finnish Meteorological Institute (FMI), containing Europe, the North Atlantic and even parts of North America, having altogether 438 × 336 grid points with a horizontal resolution of 0.2° (experiment H1). The boundaries for this model run were obtained from the ECMWF global model. In experiment H1, the operational SIC field was applied. It differed, however, dramatically from the aircraft and satellite observations. In the eastern Fram Strait, the ice edge was placed south of 78 °N (Fig. 1), while the aircraft observations clearly indicated that it was located north of 80 °N. Satellite observations, among others the high-resolution passive microwave data processed according to Kaleschke et al. (2001), were in agreement with the aircraft observations.

As the location of the ice edge is essential in our study, numerous model runs (not listed in Table 1) were performed to fix this problem. We used the technique of assimilating additional artificial SSTs into the model surface analysis in order to ensure desirable state of the sea surface (ice or open water) and thus shift the ice edge. These experiments were made with a suite of 406 × 381 grid points at the horizontal resolution of 0.08° (9 km). The model domain was chosen to cover Northern Scandinavia, Svalbard and a large part of Greenland with the Fram Strait in the centre. Analyses from H1 were used as boundaries for the higher resolution experiments. After a correct ice edge location had been reached (Fig. 1), experiment H2 was made. In addition, to check the sensitivity of HIRLAM to the aerodynamic roughness length z_0 over sea ice, a simulation with decreased z_0 (3 mm instead of 3 cm of the operational setup) was performed (experiment H3). The number of vertical levels was 40 in all HIRLAM experiments, with the lowest model level at 30–32 m above the underlying surface.

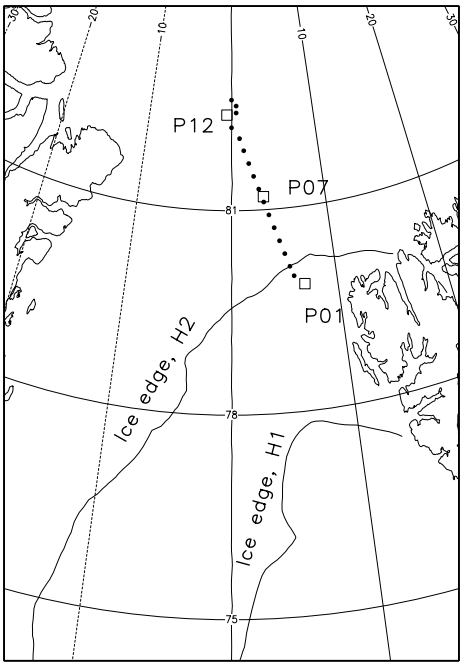

Fig. 1. Distribution of the fraction of sea ice in HIRLAM experiments H1 and H2. The lines denote the 50% ice concentration. The horizontal flight pattern is presented by dotted line and foot points of the vertical profiles P01, P07 and P12 are marked by open squares.

3.2. Two-dimensional model

3.2.1. Model description. The model used is a University of Helsinki two-dimensional hydrostatic boundary-layer model. In this application, the model has 160 points in the horizontal and 50 in the vertical; the vertical coordinate is a terrain-following modified σ; $\sigma = (p - p_t)/(p_S - p_t)$, where p is pressure, and subscripts s and t refer to the surface and model top, respectively. The horizontal grid length is 2 km and the time step accordingly 4 s. The vertical grid has quasi-logarithmic spacing with the lowest levels at approximately 1.5, 4, 8, 15 and 24 m. The upper boundary conditions are applied at 3 km, where the wind becomes geostrophic. The mesoscale flow is forced by a large-scale pressure gradient represented by the geostrophic wind. The equations of the model dry dynamics are as given in Alestalo and Savijärvi (1985), but the physical parameterizations are as in Savijärvi and Matthews (2004) with humidity, clouds and an advanced radiation scheme included. The model has previously been used in several mesoscale studies, including studies over sea ice margins with detailed validation against aircraft observations both in convective and stable conditions (Vihma and Brümmer, 2002; Vihma et al., 2003; 2005). Savijärvi and Kauhanen (2001) and Savijärvi and Amnell (2001) presented comparisons with measurements over snow and boreal forest.

The vertical diffusion coefficient K depends on the local wind shear and on the local Richardson number Ri:

$$K = l^2(dU/dz)f(Ri), \tag{1}$$

where the mixing length is given by $l = \kappa\ z/(1 + \kappa\ z/\lambda)$ with λ as its asymptotic maximum value (we use $\lambda = 30$ m; for a discussion of this value see Vihma et al., 2003) and κ as the von Karman constant (0.4). In conditions of stable stratification, the following stability function is used for momentum, heat, and moisture:

$$f(Ri)\begin{cases}\max[b, (1-5Ri)^2], & \text{for} \leq Ri < 0.2\\ b, & \text{for} \geq 0.2\end{cases}. \tag{2}$$

The parameter b represents the background turbulence in very stable conditions, and prevents K from decreasing to zero.

In all experiments except 2D5, constant values were applied for the momentum roughness length z_0 over ice. In 2D5 z_0 varied in space and was calculated on the basis of the observed momentum flux τ,

$$\tau_z = -\rho C_{Dz} V_z^2, \tag{3}$$

$$C_{Dz} = \frac{k^2}{(\log(z/z_0) - \psi_M(z/L))^2}, \tag{4}$$

where L is the Obukhov length and ψ_M is the stability function for momentum (Dyer, 1974). Calculating the drag coefficient C_{Dz} and further z_0 directly from eq. (3)–(4) would, however, result in an underestimation of the surface roughness, because it is assumed in eq. (3) that the constant-flux layer extends up to the measurement level z (approximately 24 m) of the momentum flux and wind speed. According to the observations, however, from $x = 20$–120 km the momentum flux at the height of 24 m was very close to zero. Hence, we only assume that the constant flux layer extended up to the height of 2 m. We apply eq. (3) to calculate C_{D24m} directly from the observations, and then apply an experimental equation to calculate C_{D2m} from C_{D24m}:

$$C_{D2m} = C_{Dz}\left[a + \frac{1-a}{5}z\right], \tag{5}$$

where $a = 0.1\ L^{1/4}$. Roughness length $z_0(x)$ is then solved from $C_{D2m}(x)$ using (4). A lower limit of 1×10^{-5} m, representing aerodynamically smooth surface, was applied for $z_0(x)$. Equation (5) is derived from Garbrecht et al. (2002) tuning the parameters so that the median z_0 over sea ice is 1 mm (Garbrecht et al. (2002) presented an equation for C_{D10m}, but in this case we cannot even assume that the constant-flux layer reaches the height of 10 m). We calculate the thermal roughness length $z_T(x)$ over ice according to Andreas (1987) and over the open ocean set it to 0.5 z_0 (a simplification, which can be derived by combining the results of De Cosmo et al. (1996) and Taylor (2002)). Over the open ocean z_0 was 1×10^{-4} m in all experiments.

The long-wave radiation is calculated using a six-band emissivity scheme, which is based on the well-tested code of the ECMWF model (Morcrette, 1991) but further improved (Savijärvi and Räisänen, 1998) to allow good accuracy with the high vertical resolution of our mesoscale model. The scheme assumes that clouds are of mixed-phase with the portions of

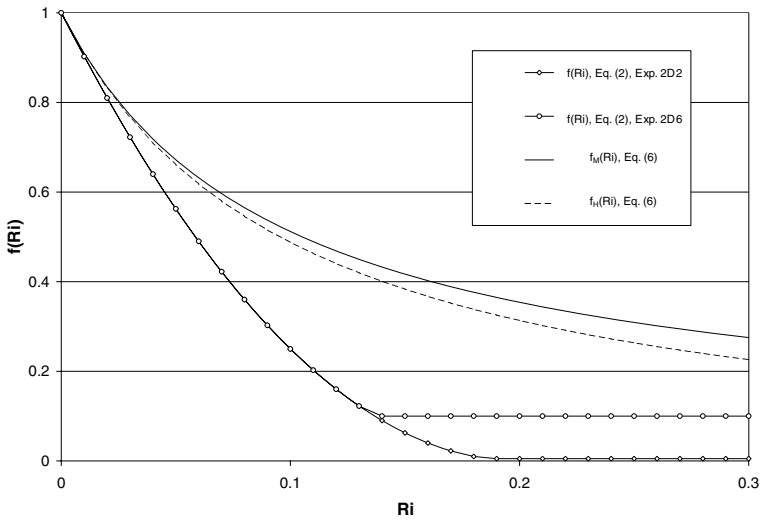

Fig. 2. Comparison of the stability functions.

liquid water and ice depending on the temperature. The shortwave radiation is calculated with a four-band two-stream scheme (Savijärvi et al., 1997). To save computer time, the full radiative transfer is solved every 180 seconds.

The conductive heat flux through the ice and snow is calculated applying a 7-layer scheme (four layers in snow and three in ice). We apply 2.0 m for the ice thickness and 0.3 m for the snow thickness (h_i and h_S, respectively), which are typical for the Fram Strait in late winter. With such relatively large values, the conductive heat flux is fortunately not too sensitive to h_i and h_S (Makshtas, 1991). For the thermal conductivities of snow and ice we use 0.25 and 2.1 W m^{-1} K^{-1}, respectively (Sturm et al., 2002). The ice bottom temperature is kept at -1.8 °C. The snow surface temperature is solved from the balance of the turbulent, radiative and conductive heat fluxes.

3.2.2. Experiment setup. The model domain covered the region $-48 \leq x \leq 266$ km. The simulations were started on 12 March 1998 at 00 UTC and run for 12 h. We prescribed the inflow boundary conditions at $x = -48$ km for air temperature and moisture according to the observed vertical profiles at P01. The geostrophic wind components (u_G and v_G) were set according to the large-scale pressure gradient and the aircraft observations above the boundary layer: $u_G = 14.0$ m s^{-1}, $v_G = 0$ m s^{-1}. The initial wind profile was calculated according to the Ekman-Taylor spiral. Comparing the aircraft observations in the beginning and end of the flight mission, it appeared that the situation remained practically stationary during this 2.5 h period. The time scale of the observed warm-air advection over the sea ice was, however, much longer. On the basis of the observed wind field and results of H2, we can estimate that the air mass that was observed over the ice at $x = 270$ km had been at the ice edge approximately 10–12 h earlier. According to the results of H2, the air at P01 became colder and dryer during the 12-h period prior the aircraft observations. We, therefore, prescribed time-dependent inflow boundary conditions, which were based on the observations at P01 and the temporal evolution based on H2. The following inflow boundary conditions were applied for air potential temperature *(θ)* and specific humidity *(q)*: $\partial\theta(z)/\partial t = -1.2 \times 10^{-5}$ K s^{-1} and $\partial q(z)/\partial t = -2.8 \times 10^{-9}$ s^{-1}. The wind profile at the inflow boundary was kept constant during the time integration.

In experiments 2D1, 2D6 and 2D7 (Table 1), we prescribed the surface potential temperature $\theta_S(x,t)$ according to the observations from the low-level flight legs. By prescribing $\theta_S(x,t)$ we can validate the model results with respect to the ABL evolution without introducing additional inaccuracy caused by a bias in $\theta_S(x,t)$. The effects of errors in surface temperature can be studied by comparing the results of 2D1 and 2D2. The purpose of 2D3 is to study how important it is to take into account the fraction of the surface covered by thin ice (refrozen leads). The aircraft observations indicated that with $x > 100$ km there were frequent areas of grey ice, which covered approximately 10% of the surface. Hence, in 2D3 for $x > 100$ km, we set every tenth grid cell as grey ice with a thickness of 5 cm without snow cover.

Experiments 2D4 and 2D5 were made to test the model sensitivity to z_0. In 2D4, 1 mm was applied, which is the most commonly used value for z_0 over sea ice. Spatial variations in z_0 can, however, have important effects on the wind and temperature fields (Vihma et al. 2003), and this was taken into account in 2D5, where z_0 was based on eq. (3)–(5). The purpose of 2D6 and 2D7 is to study the sensitivity of the model results to the stability dependence of turbulent mixing; comparison of 2D1 and 2D6 demonstrate the model's sensitivity to parameter b in eq. (2). In 2D7 the same stability dependence as in HIRLAM (and in the ECMWF model) was applied, that is, instead of eq. (2) the following equation was applied (Undén et al., 2002):

$$f_M(Ri) = \frac{1}{1 + \dfrac{10Ri}{\sqrt{1+Ri}}}, \qquad f_H(Ri) = \frac{1}{1 + 10Ri\sqrt{1+Ri}}, \tag{6}$$

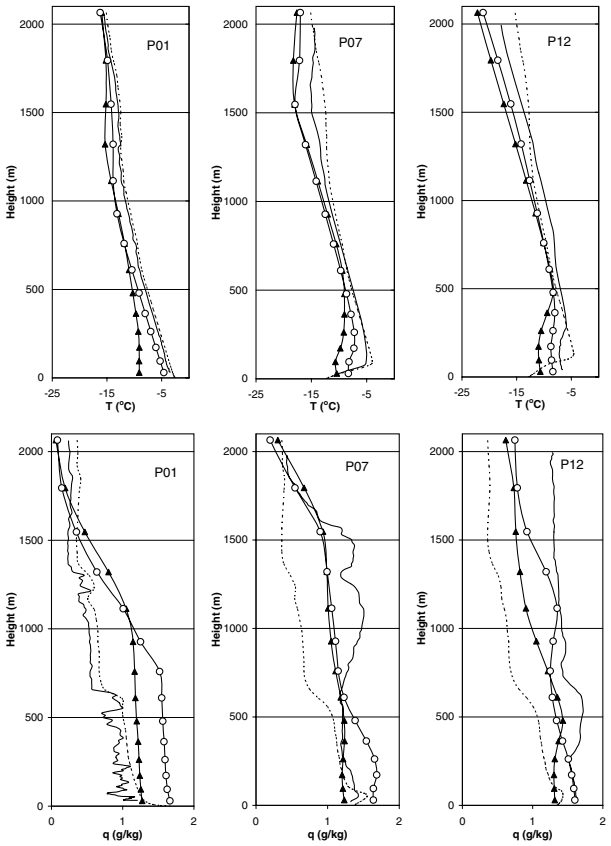

Fig. 3. Vertical profiles P01, P07 and P12 of observed (continuous line) and modelled (H1: lines with triangles, H2: lines with open circles, 2D2: dashed lines) temperature T and specific humidity q.

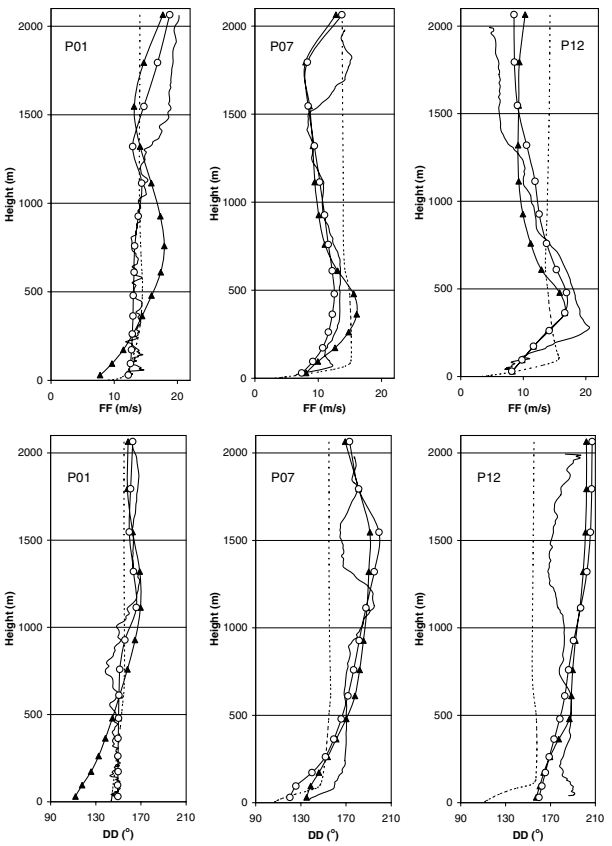

Fig. 4. Vertical profiles P01, P07 and P12 of observed (continuous line) and modelled (H1: lines with triangles, H2: lines with open circles, 2D2: dashed lines) wind speed FF and wind direction DD.

where the subscripts M and H refer to the stability functions for momentum and heat, respectively. Comparison of the stability functions based on eq. (2) and (6) is shown in Fig. 2.

4. HIRLAM results

Comparisons of model results against the observations of vertical profiles of air temperature, specific humidity, wind speed and wind direction are shown in Figs. 3 and 4. Here and henceforth, the HIRLAM output is 6 h forecast, valid at 12 UTC, 12 March 1998, and the values are taken from the grid point nearest to the true measurement location.

The results of H1 are strongly affected by the erroneous location of the ice edge. At P1, which was over the open sea in reality but over sea ice in H1, the ABL is stably stratified and too cold (Fig. 3), and the ABL wind speed is too low and, due to the larger roughness of sea ice, the wind has turned too much towards the centre of the low (Fig. 4). The air temperature at the lowest model level has an almost uniform horizontal distribution (Fig. 5). The only positive aspect in H1 is that the air humidity agrees better with the observations, except at P12, than in H2. This seems to be due to the compensating effect of errors: the excessive sea ice cover strongly reduces evaporation, while HIRLAM has a general tendency to produce too moist ABL (Pirazzini et al., 2002; Rodríguez et al., 2003).

Next, we discuss the results of H2. One can observe a general tendency of the model to slightly underestimate the temperature in the whole observed ABL while, in contrast, the near-surface inversion is missed in profile P07 at $x = 101$ km, associated with too high surface temperature in the model. Specific humidity is overestimated by HIRLAM already over the open sea. Along the flight pattern from the open sea to ice and further towards northwest the measured moisture increases and in P12, where both in the model and observations a closed cloud deck was present, coincides fairly well in the lowest 200–300 m.

The observed wind speed profile over ice at P12 ($x = 258$ km) includes a low-level jet (LLJ) at the height of 300 m. At the ice edge, the ABL stratification has increased yielding a strong decrease in the turbulent mixing. Hence, at the top of the stable boundary layer, the ageostrophic wind component has started inertial oscillations, and we can estimate that it had become parallel to the geostrophic wind approximately at the time of $1/3 \times 12\,\mathrm{h}\,/\sin(\phi)$ after passing the ice edge, where ϕ is the latitude (Thorpe and Guymer, 1977; Vihma and Brümmer, 2002). With

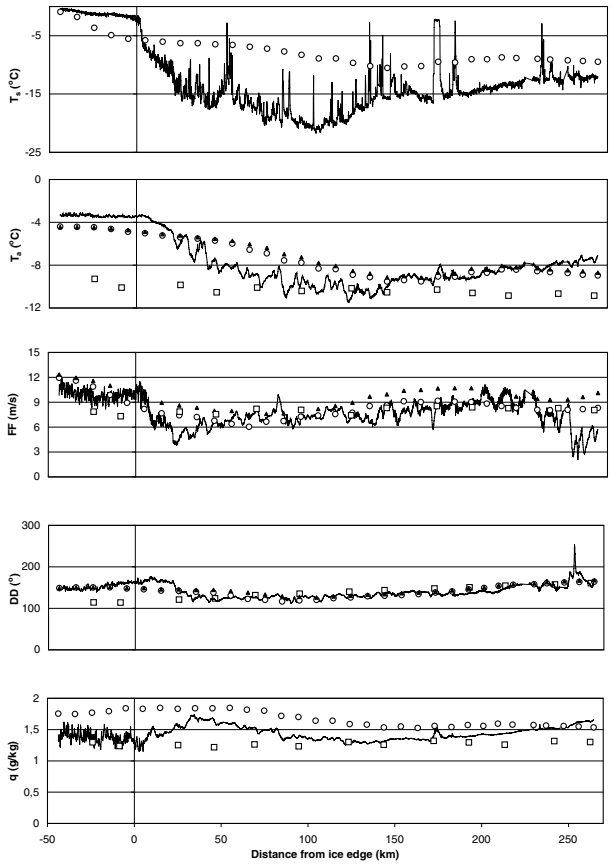

Fig. 5. Horizontal distribution of observations and HIRLAM results along the flight pattern: surface temperature T_s, air temperature T_a, wind speed FF, wind direction DD and specific humidity q. Measured values are given by thin lines, and results of model experiments by open squares (H1), open circles (H2), and filled triangles (H3). In x-axis the distance from ice edge is based on the observations.

the observed wind speeds, this time (4.1 h) corresponds to a travel distance of approximately 250 km, which could explain the LLJ at the top of the ABL at P12. In H2, the evolution of the wind profile from P01 via P07 to P12 agrees well with observations (Fig. 4), although the LLJ at P12 is not as pronounced and has its core at a higher elevation, corresponding to the top of the stable boundary layer in H2. In the HIRLAM experiments, colder air locates to the right of the wind vector at P01, P07 and P12 in H1, and at P07 and P12 in H2. Hence, also baroclinicity contributes to the generation of the LLJ. In the observations, the situation at P12 is reversed with the front just northwest of P12.

The aircraft observations also included a vertical profile P13 some 20 km west of P12. P13 located north-west of a sharp temperature front, and the ABL was up to 12 K colder with a surface-based temperature inversion under cloudy skies. The formation of the inversion can be explained by the downstream advection of warm air above the cold Arctic air, supported by observed very weak winds in the cold air mass (Brümmer and Thiemann, 2002, their Fig. 3). In HIRLAM, however, this front was located more in the west, close to the northeastern corner of Greenland, and there was practically no difference in the air mass between the locations of P12 and P13. Comparisons against observations at P13 are thus not shown.

The horizontal distributions of a number of basic measured and predicted meteorological quantities along a more than 300 km long flight are shown in Fig. 5. Here the modelled values of air temperature, humidity and wind characteristics are directly from the lowest model level. In H2, the air temperature T_a is reproduced reasonably well: the bias and root-mean-square error (RMSE) of each experiment are shown in Table 2. The surface temperature T_s is, however, too high. This can be explained at least partly by too large long-wave radiation and clouds in model, but other effects are not excluded. This in turn causes strong underestimation of temperature difference $T_a - T_s$. Wind speed and wind direction were also reproduced fairly well (bias 0.5 m s^{-1} and RMSE 1.4 m s^{-1} for the wind speed in H2), showing initial decrease of the wind speed (and wind backing) over ice due to changes in stability and roughness. Moving further downstream, with growing of a shallow stable IBL, wind speed and wind direction values (wind veering) increase slowly again (Brümmer and Thiemann, 2002). In H2, the specific humidity at the lowest model level is overestimated already over the open sea and further over the sea ice until $x \approx 250$ km. Both air temperature and humidity strongly depended on the sea ice distribution. Thus, H1 with excessive sea ice cover produced too cold air with nearly constant T_a of $-10 \ldots -11$ °C and, on the contrary to H2, also air humidity was underestimated over sea ice. Decreasing the ice roughness length by factor 10 in H3 has a very small influence on the air temperature (Fig. 5; Table 2). Resulting wind speed over ice, as expected, slightly increased (by 1–2 m s^{-1}) but compared to measurements yielded worse results.

Results of observed and modelled vertical fluxes of latent heat (E), sensible heat (H), downward shortwave (S↓) and longwave (L↓) radiation, net radiation (R) and albedo (α) are displayed in Fig. 6. The HIRLAM latent heat flux is over the open sea strongly positive (upward) but reduces significantly downstream along the flight leg. Over ice, modelled E remains slightly positive, compared with observed values close to zero. Modelled and measured sensible heat fluxes behave basically in similar way but over ice the modelled H is underestimated by 10–30 W m^{-2}. That can be partly explained by the fact that all HIRLAM fluxes are surface fluxes (the constant-flux layer is assumed up to the lowest model level) but the observations are from the flight altitude of approximately 24 m (see Section 5). Downward long-wave and short-wave radiation fluxes reflect strong dependence on the presence of clouds. Thus, HIRLAM predicted overcast conditions for almost all the study region, except for a small area approximately 150 km from the ice edge. In the observations, however, the situation was mostly cloudless with closed altostratus cloud sheet appearing only in the farther northwest part of the flight leg ($x \geq 250$ km). This effect can be seen as

Table 2. Model validation statistics over the sea ice zone (x > 0, including leads and thin ice)

Parameter		Experiment									
		H1	H2	H3	2D1	2D2	2D3	2D4	2D5	2D6	2D7
V	Bias	0.7	0.5	1.8	0.6	0.4	0.5	1.5	2.1	0.7	0.4
	RMSE	1.3	1.4	2.3	1.7	1.6	1.6	2.1	3.1	1.8	1.5
T_s	Bias	*	6.0	6.0	0.0	2.3	0.6	1.6	0.1	0.0	0.0
	RMSE	*	6.9	6.9	0.0	4.1	3.8	3.9	3.7	0.0	0.0
T_a	Bias	−1.9	0.4	0.7	−2.4	−1.0	−2.3	−1.0	−0.3	−1.9	−2.2
	RMSE	2.3	1.4	1.6	2.7	1.9	3.3	1.0	1.5	2.3	2.5
q	Bias	−0.19	0.20	0.20	−0.07	0.10	−0.04	0.06	0.16	−0.03	−0.07
	RMSE	0.22	0.25	0.24	0.14	0.17	0.20	0.15	0.21	0.13	0.15
τ	Bias	*	*	*	59	64	59	50	45	59	75
	RMSE	*	*	*	63	66	61	53	55	62	77
H	Bias	*	−23	*	−17	−15	−18	−14	−10	−19	−26
	RMSE	*	25	*	20	17	20	16	14	23	31
E	Bias	*	4	*	−1	0	−2	−0	−0	−1	−1
	RMSE	*	5	*	5	5	5	5	6	5	5

*Model output not available.

too large values of modelled L↓ and too small S↓, except in the clear region of the model (Fig. 6). Comparing with observations, the HIRLAM ice albedo is too small, with almost constant value around 0.6. This tends to balance the effect of too small downward shortwave radiation. Radiation balance R was reproduced by model fairly well over the open sea but over ice we see, as expected, a strong correlation with the modelled total cloud cover.

5. Two-dimensional model results

5.1. Vertical profiles

We show the vertical profiles only on the basis of experiment 2D2: the sensitivity to surface temperature, roughness, and stability formulations is better illustrated comparing the near-surface horizontal distributions (Sections 5.2 and 5.3). The vertical profiles of air temperature, specific humidity as well as wind speed and direction are shown in Figs. 3 and 4. The profiles are presented at P01, P07 and P12: at P01 the model fields were prescribed by observations and at P13, as in the case of HIRLAM, there was no distinguishable difference from P12.

In the 2D model, the situation remained cloud-free over the whole model domain. The development of the surface-based temperature inversion at P07 is very well reproduced (Fig. 3): this is clearly better than in HIRLAM (where it was cloudy at P07). At P12, the ABL is somewhat thicker than at P07, but due to lack of clouds in the 2D model, the observed significant thickening does not take place. The humidity profiles in the 2D model differ from the observations, and suggest that the situation has not been entirely stationary with respect to air humidity. In the 2D model, the specific humidity keeps approximately constant downstream over the ice, with small changes in the lowermost 100 m. In the observations, however, the specific humidity increases from P07 to P12 in the layers below 600 m and above 1600 m. In addition, there is a strong increase from P01 to P07 (Fig. 3). We interpret these as signs of non-stationary conditions: at the time of its arrival to the ice edge, the air mass that was observed at P07 and P12 must have been moister than the air mass observed at P01. With the time-dependent inflow boundary conditions, it should have been possible to reproduce the observations. The results of H2, which formed the basis for the inflow $\partial q(z)/\partial t$ in the 2D model, were, however, too inaccurate with respect to air humidity. The 2D model reproduces a low-level wind maximum at P12, but it locates too low and is weaker than in the observations.

5.2. Sensitivity to surface roughness

The observed and modelled horizontal profiles of wind speed are shown in Fig. 7. The model produces the best wind speed distribution when a constant value of 1 cm is used for z_0 (2D2). Experiment 2D4 with $z_0 = 1$ mm somewhat overestimates the wind speed, while 2D5 based on eq. (3) to (5) results in strong overestimation in the region from $x = 20$ to 120 km, where the observed momentum flux was close to zero. For $x > 0$, the biases are 0.4, 1.5 and 2.1 m s^{-1} for 2D2, 2D4 and 2D5, respectively (Table 2). Compared to 2D2, removal of thin ice (2D3) and prescription of the surface temperature (2D1) had no or minor effects on the bias and RMSE of the wind speed. None of the model experiments reproduced the sharp drop in the wind speed at $x = 248$ km.

The observed and modelled horizontal profiles of the momentum flux are shown in Fig. 8. The aircraft observations are from

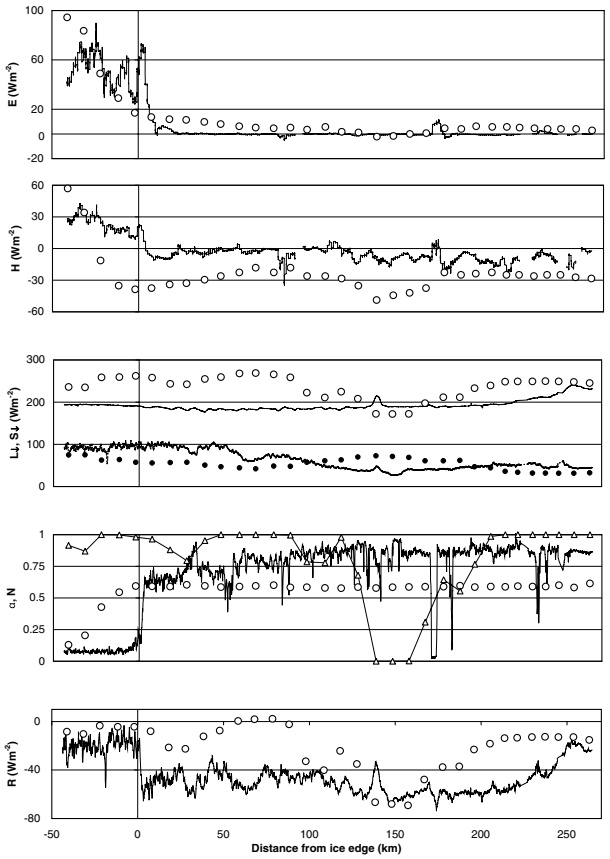

Fig. 6. As Figure 5 but for latent heat flux E, sensible heat flux H, downward long-wave $L\downarrow$ and short-wave $S\downarrow$ radiation fluxes, albedo α and net radiation flux R. Measured values are given by thin lines, except $S\downarrow$ by a thick line. Results of HIRLAM experiment H2 are given by open circles, except $S\downarrow$ by filled circles. The line with open triangles represents total cloud cover N distribution in H2.

a mean height of 24 m, and the model results are presented both for 24 m (fifth atmospheric model level) and the surface. The vertical divergence of the momentum flux is clearly seen in the model results: over sea ice the flux at the height of 24 m is on average 64% of the surface flux, while the ratio is 84% over the open ocean. The flux at 24 m is closer to the observations in all experiments 2D2, 2D4, and 2D5. This demonstrates that in conditions of stable stratification even aircraft observations from altitudes as low as 20–30 m should not be interpreted as representing surface momentum flux.

The model reproduces the horizontal decrease in the momentum flux from the open sea-to-sea ice. Although z_0 is larger over sea ice than over the open sea (except in some regions in 2D5), the stability effect dominates the momentum flux, seen as a clear decrease over sea ice. In experiments 2D2 and 2D4, the momentum flux is, however, too large over sea ice. In 2D5, in which the distribution of z_0 was based on the observed momentum flux and wind speed, the near-zero momentum flux at $x = 20$ to 120 km was very well reproduced, but the wind speed was overestimated in the same region. Although several additional model experiments were made (not listed in Table 1), we did not find a z_0 distribution that would yield best results simultaneously for the wind speed and momentum flux.

5.3. *Temperature, heat fluxes and stratification effects*

The observed and modelled horizontal profiles of air and surface temperature are shown in Fig. 9, where we present results from model runs focusing on the treatment of snow and ice thermodynamics. With the surface temperature prescribed (2D1), the model tends to cool the air mass too rapidly. When the surface temperature is simulated with a realistic ice thickness distribution (2D2), the air temperature distribution is very good until $x = 170$ km, but this is accompanied with too high surface temperature, that is, compared to the surface temperature, the air mass again cools too fast. Further downstream the observations indicated clouds, but the 2D model experiments remained cloud free, probably due to inaccuracy in estimating the temporal change in the inflow boundary conditions. Due to the dominating effect of erroneous cloud cover, we do not show detailed comparison of radiative fluxes. Without thin ice in the model domain (2D3), the 24-m air temperature became up to 2.7 K colder (at $x = 245$ km) than with a realistic ice thickness distribution. The surface temperature was naturally higher in the grid squares covered by thin ice but, via the effect of turbulent heat exchange between the thin ice, air, and thick ice, also the surface temperature of thick ice was increased (by up to 3 K) when thin ice was included in the domain.

Comparing RMSE in experiments 2D2–2D5 (Table 2), the surface temperature was approximately equally well reproduced. The smallest bias was reached in 2D5 (see below) and 2D3: in the latter the overestimation and underestimation in various regions compensated each other (Fig. 9). On the basis of RMSE, the 24-m air temperature was best reproduced in 2D4 with $z_0 = 1$ mm, while 2D3 without thin ice was the worst. Also, ranked on the basis of the sum of RMSE for surface and air temperature, 2D4 was the best and 2D3 the worst experiment.

The turbulent fluxes of sensible and latent heat are shown in Figs. 10 and 11. As in the case of the momentum flux, the magnitudes of sensible and latent heat fluxes were strongly reduced with altitude. Over thick sea ice, the sensible heat flux at the height of 24 m was on average 60% of that at the surface, while over thin ice and leads the ratio was 22% on average, but as low as 6% over the 4-km-wide lead at $x = 167$–171 km. For the latent heat flux, the corresponding numbers were 23%, 28%, and 13%. It is noteworthy that the signal of leads and thin ice in the observed heat fluxes is very small: even the 4 km lead can hardly be detected on the basis of the observed sensible heat flux, which was 5 W m^{-2} compared to -10 and -20 W m^{-2} immediately upwind and downwind, respectively. In the observed latent heat flux, which shows less variability elsewhere, the signal was

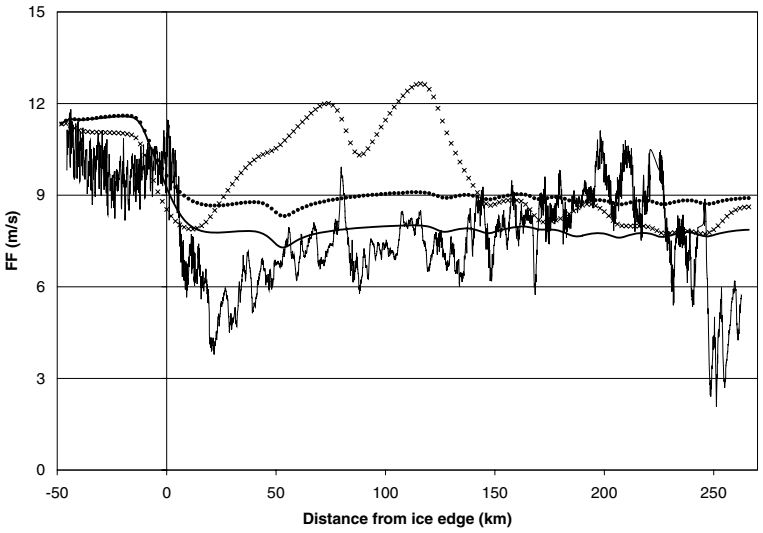

Fig. 7. Observed (thin line) and modelled wind speed in experiments 2D2 (thick solid line), 2D4 (filled circles) and 2D5 (crosses).

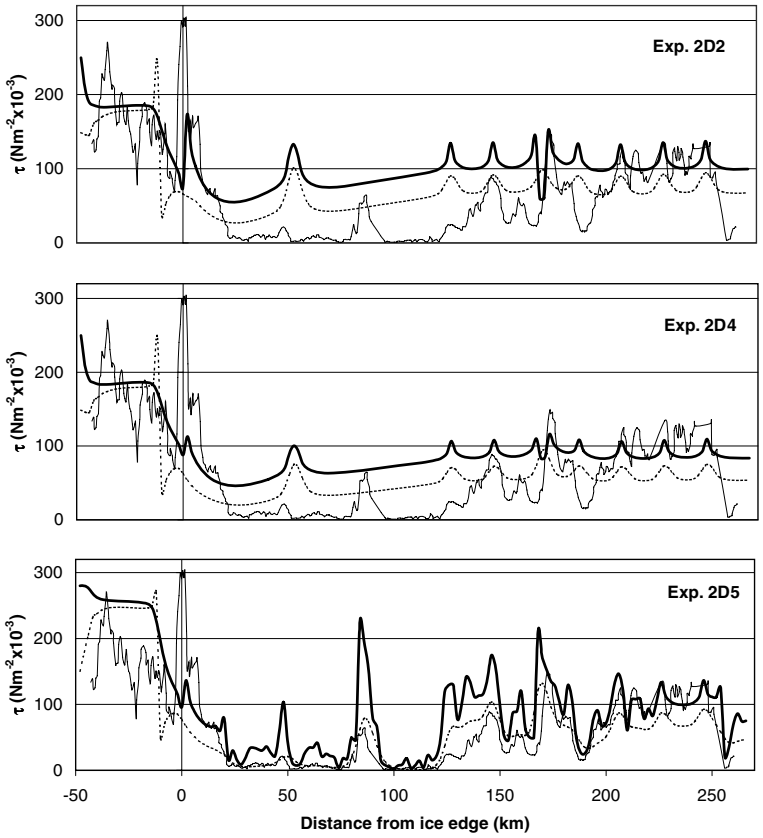

Fig. 8. Observed (thin lines) and modelled momentum flux τ in experiments 2D2, 2D4 and 2D5. The model results are presented for the flux at the surface (thick solid lines) and at the height of 24 m (dashed lines).

10 W m^{-2} compared to the upwind and downwind values of 0 and -3 W m^{-2}, respectively. The modelled fluxes at the height of 24 m over the 4-km lead agreed reasonably well with observations (Figs. 10 and 11), although the fluxes were overestimated in 2D1 and 2D5. The large flux divergences over leads are related to low penetration of convective plumes. The penetration height is sensitive to the background stratification (Esau, 2007). In our case it was particularly strong: upwind of the 4-km lead, the potential temperature increased by 9 K in the lowermost 100 m.

In 2D5, z_0 was extremely small, 1×10^{-5} m, in the region 20 km $< x <$ 100 km. We do not consider this value realistic for sea ice, but it is interesting to note that in this region the best surface temperature, momentum flux, as well as sensible and latent heat fluxes together with almost the best 24-m air temperature were obtained in an experiment where the atmosphere was

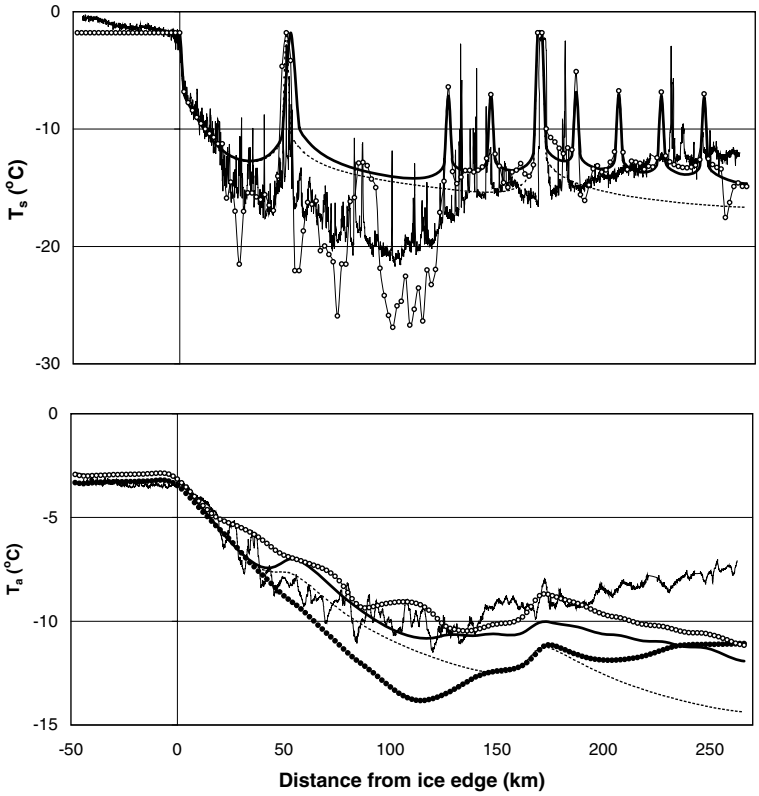

Fig. 9. Observed (thin lines) and modelled surface temperature T_s (upper panel) and 24-m air temperature T_a (lower panel) in experiments 2D1 (filled circles), 2D2 (thick solid lines), 2D3 (dashed lines), and 2D5 (lines with open circles).

practically frictionally decoupled from the underlying surface (Figs. 9–11)

The results from model runs 2D6 and 2D7 with modified stability functions can be summarized as follows. Increasing the level of background turbulence, that is, changing b from 0.005 (2D1) to 0.1 (2D6), resulted in a reduction of the bias of the 24-m air temperature by 0.5 K, but the turbulent fluxes were not much affected (Table 2). Using the HIRLAM stability functions (2D7), which yield much weaker reduction of turbulent mixing with increasing stability (Fig. 2), the results for air temperature were only slightly improved, but the results for turbulent fluxes of momentum and sensible heat simultaneously became worse with too large magnitudes (directed downwards over the ice). Compared to 2D1, changes in the stability effects on turbulence (2D6 and 2D7) had minor effects on the bias and RMSE of the 24-m wind speed when averaged over the sea ice zone (Table 2). In the region of the largest air-surface temperature difference ($x = 20$–120 km), the influence on the wind speed was, however, up to 1 m s^{-1}. The enhanced turbulent mixing generated veering of the 24-m wind, but the maximum effects were only 5°.

6. Summary and conclusions

This study demonstrated that errors in the location of the sea ice edge can have dramatic influences in the results of operational numerical weather prediction (NWP) models for the ABL. Improving the information on the ice conditions yields a significant improvement in the model results (as demonstrated by the comparison of H1 and H2). On the basis of the results, we strongly recommend that frequently updated satellite-based information on the sea ice extent should be applied in operational models.

In addition to the location of the ice edge, inaccurate information on the ice concentration within the sea ice zone can yield large errors in numerical models (Vihma and Brümmer, 2002; Drusch, 2006; Valkonen et al., 2008). In this study, we did not specifically test this, but the effects of ice thickness distribution became evident. Ignoring the new, thin ice formed in refrozen leads, the negative bias in the 24-m air temperature increased locally by almost 3 K. In the Arctic winter, leads typically remain open only for a few hours. Hence, the area fraction of thin ice may be even more important than the fraction of open water (i.e. the ice concentration). Adding a thin ice component in a tile method for flux aggregation is, in principle, straightforward, but taking it into account in operational modelling would require a method to accurately estimate the thin ice fraction. At the moment, for small (less than 10%) fractions of thin ice, there are no accurate methods available for operational use, but the ice type classification on the basis of space-born altimetry and Synthetic Aperture Radar data has potential for that (Kwok et al., 2006).

In the HIRLAM runs with a reasonable ice edge location (H2 and H3), the main errors were the wrong location of the

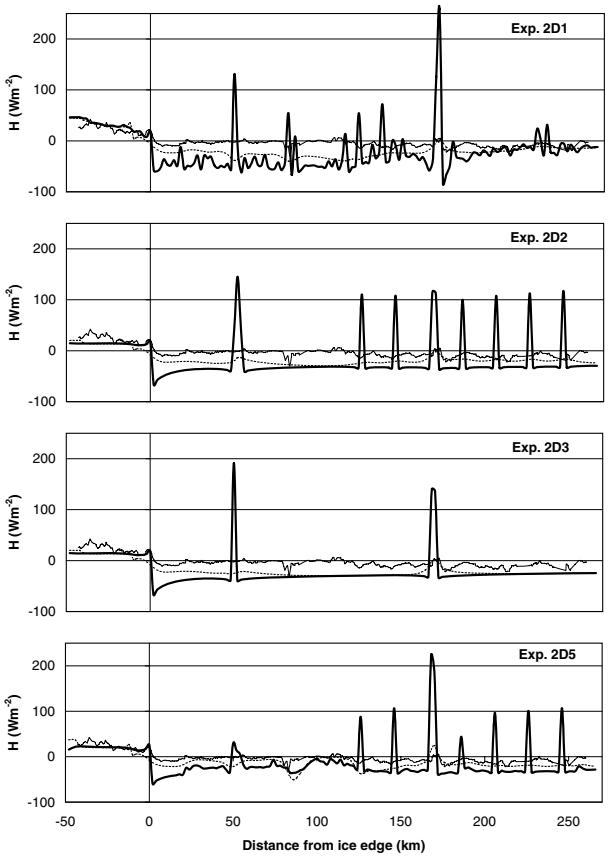

Fig. 10. Observed (thin lines) and modelled sensible heat fluxes H in experiments 2D1, 2D2, 2D3 and 2D5. The model results are presented for the flux at the surface (thick solid lines) and at the height of 24 m (dashed lines).

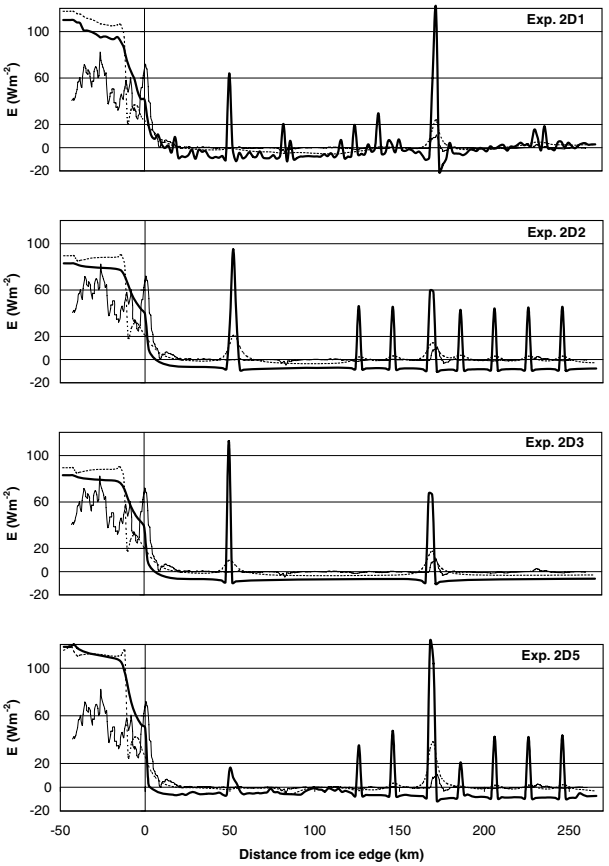

Fig. 11. Observed (thin lines) and modelled latent heat fluxes E in experiments 2D1, 2D2, 2D3 and 2D5. The model results are presented for the flux at the surface (thick solid lines) and at the height of 24 m (dashed lines).

synoptic-scale front observed between P12 and P13 and the excessive humidity and cloud cover, which yielded too high surface temperature. The excessive humidity in the ABL has been identified as a common problem in HIRLAM (Pirazzini et al., 2002; Rodríguez et al., 2003). In this case, it was not concretely related to the modelling of the ABL over sea ice, but the air humidity was far too high in the inflow region over the open ocean.

Modelling of the thermodynamic coupling between the snow surface and near-surface air was a problem for both HIRLAM and the 2D model. In both models, a good 24-m air temperature was associated with a too high surface temperature, and with the surface temperature prescribed the air mass cooled too much in the 2D model. From the point of view of wind speed and air temperature, H2 was as good as any of the 2D model experiments, but this was related to simultaneous large errors in the surface temperature in H2.

The 2D model experiments were successful in reproducing the decrease of momentum flux downwind of the ice edge, as the effects of increased stratification dominated over the increased surface roughness. The simultaneous reduction of near-surface wind speed was reproduced in most model experiments. The LLJ observed 258 km downstream of the ice edge was, however, not well reproduced by the 2D model. The study demonstrated that the commonly used value of 1 mm for the roughness length of sea ice is not always the best choice compared with $z_0 = 1$–3 cm, which performed better with respect to the near surface wind speed both in HIRLAM and the 2D model. In the case studied, the ice pack further from the ice edge ($x > 120$ km) was heavily ridged, but probably not much different from average multiyear sea ice in the Arctic. Simulation of this single case cannot be a basis of firm conclusions on the optimal z_0 for NWP and climate models, but it suggests that sensitivity tests with more extensive validation would be needed. This need was particularly demonstrated by the observations and model results from the region 20 km $< x <$ 120 km, where the observed momentum flux was close to zero, and the best surface temperature and turbulent fluxes (but not the wind speed) were obtained by applying an unrealistically small z_0. The effects of sea ice z_0 are not only restricted to the near-surface wind speed, but also on the frictional convergence and evolution of the large-scale pressure field.

The model results showed that aircraft observations from altitudes as low as 20–30 m should not be interpreted as representing surface fluxes. In the case of sensible and latent heat fluxes, this was particularly clear over leads: the modelled fluxes at the surface exceeded 100 W m^{-2}, although the measured and modelled flux at the height of 24 m was only 5–15 W m^{-2}. This is due to the stable background stratification, which prevents the heat plumes rising to high altitudes. The vertical differences were large also over stably stratified sea ice. HIRLAM strongly overestimated the magnitude of turbulent fluxes of momentum and heat. In the case of the sensible heat flux, the errors in HIRLAM were above all related to the too small air-surface temperature difference, but the overestimation was partly due to the fact that the lowest model level is as high as 30 m, and the constant flux layer is assumed up to that level.

7. Acknowledgments

The results presented are an outcome of the DAMOCLES project (grant 18509), funded by the 6th Framework Programme of the European Commission (grant LU 818/1-1). Two anonymous reviewers are acknowledged for their remarks and suggestions that helped us to improve the manuscript.

References

Alestalo, M. and Savijärvi, H. 1985. Mesoscale circulations in a Hydrostatic Model: Coastal convergence and orographic lifting. *Tellus*. **37A**, 156–162.

Andreas, E. L. 1987. A theory for the scalar roughness and the scalar transfer coefficients over snow and sea ice. *Bound. Lay. Met*. **38**, 159–184.

Andreas, E. L., Tucker III, W. B. and Ackley, S. F. 1984. Atmospheric boundary-layer modification, drag coefficient, and surface heat flux in the Antarctic marginal ice zone. *J. Geophys. Res*. **89**, 649–661.

Bennett, T. J. Jr. and Hunkins, K. 1986. Atmospheric boundary layer modification in the marginal ice zone. *J. Geophys. Res*. **91**, 13033–13044.

Bradley, R. S., Keimig, F. T. and Diaz, H. F. 1992. Climatology of surface-based inversions in the North American Arctic. *J. Geophys. Res*. **97**, 15699–15712.

Brümmer, B. 1996. Boundary-layer modification in wintertime cold-air outbreaks from the arctic sea ice. *Bound. Lay. Met*. **80**, 109–125.

Brümmer, B. and Thiemann, S. 1999. Field Campaign ACSYS 1998: Aircraft Measurements in Arctic On-Ice Air Flows. *Ber. aus dem Zentrum f. Meeres- u. Klimaforschung, Reihe A* **32**, 35 pp.

Brümmer, B. and Thiemann, S. 2002. Arctic wintertime on-ice air flow. *Bound. Lay. Met*. **104**, 53–72.

Brümmer, B., Busack, B. and Hoeber, H. 1994. Boundary-layer observations over water and arctic sea ice during on-ice air flow. *Bound. Lay. Met*. **68**, 75–108.

Brümmer, B., Schröder, D., Launiainen, J., Vihma, T., Smedman, A.-S., and co-authors 2002. Temporal and spatial variability of surface fluxes over the ice edge zone in the northern Baltic Sea. *J. Geophys. Res*. **107**, doi:10.1029/2001JC000884.

Cats, G. 2005. Reference system status December 2005. *HIRLAM Newsl* **49**, 105–106, HIRLAM-6 Project, c/o Per Undén, SMHI, S-601 76 Norrköping, SWEDEN.

Cheng, B. and Vihma, T. 2002. Modelling of sea ice thermodynamics during warm-air advection. *J. Glaciol*. **48**, 425–438.

Cuxart, J., Bougeault, P. and Redelsberger, J. L. 2000. A turbulence scheme allowing for mesoscale and large-eddy simulations. *Quart. J. Roy. Meteorol. Soc*. **126**, 1–30.

De Cosmo, J., Katsaros, K. B., Smith, S. D., Anderson, R. J., Oost, W. A. and co-authors. 1996. Air-sea exchange of water vapor and sensible heat: The humidity exchange over the sea (HEXOS) results. *J. Geophys. Res*. **101**, 12001–12016.

Drusch, M. 2006. Sea ice concentration analyses for the Baltic Sea and their impact on numerical weather prediction. *J. Appl. Meteorol. Climatol*. **45**, 982–994.

Dyer, A.-J. 1974. A review of flux-profile relationships. *Bound. Lay. Met*. **7**, 363–372.

Esau, I. N. 2007. Amplification of turbulent exchange over wide Arctic leads: Large-eddy simulation study. *J. Geophys. Res*. **112**, D08109, doi: 10.1029/2006JD007225.

Fairall, C. W. and Markson, R. 1987. Mesoscale variations in surface stress, heat fluxes, and drag coefficient in the marginal ice zone during the 1983 marginal ice zone experiment. *J. Geophys. Res*. **92**, 6921–6932.

Garbrecht, T., Lüpkes, C., Hartmann, J. and Wolff, M. 2002. Atmospheric drag coefficients over sea ice – validation of a parameterization concept. *Tellus* **54A**, 205–219.

Glendening, J. W. 1994. Dependence of boundary layer structure near an ice-edge coastal front upon geostrophic wind direction. *J. Geophys. Res*. **99**, 5569–5581.

Guest, P. S., Glendening, J. W. and Davidson, K. L. 1995. An observational and numerical study of wind stress variations within marginal ice zones. *J. Geophys. Res*. **100**, 10887–10904.

Homleid, M., Albertsen, J., Eastwood, S. and Vignes, O. 2005. Daily updates of sea surface temperature and sea ice concentration fields based on O&SI SAF data in HIRLAM at the Norwegian Meteorological Institute. *HIRLAM Newsletter* **48**, 82–91, HIRLAM-6 Project, Available from SMHI, S-60176 Norrköping, Sweden.

Inoue, J., Kawashima, M., Fujiyoshi, Y. and Wakatsuchi, M. 2005. Aircraft observations of air-mass modification over the Sea of Okhotsk during sea-ice growth. *Bound. Lay. Met*. **117**, 111–129.

Kaleschke, L., Lüpkes, C., Vihma, T., Haarpainter, J., Bochert, A. and co-authors. 2001. SSM/I sea ice remote sensing for mesoscale ocean-atmosphere interaction analysis. *Canadian J. Remote Sensing* **27**, 526–536.

Kantha, L. H. and Mellor, G. L. 1989. A two-dimensional coupled ocean-ice model to the Bering sea marginal ice zone. *J. Geophys. Res*. **94**, 10921–10935.

Källén, E. 1996. HIRLAM documentation manual. System 2.5. *HIRLAM Technical Report*, Available from SMHI, S-60176 Norrköping, Sweden, 178 p. + 55 p. appendix.

Kwok, R., Cunningham, G. F., Zwally, H. J. and Yi, D. 2006. ICESat over Arctic sea ice: Interpretation of altimetric and reflectivity profiles. *J. Geophys. Res*. **111**, doi: 10.1029/2005JC003175.

Lenderink, G. and De Rooy, W. 2000. A robust mixing length formulation for a TKE-l turbulence scheme. *HIRLAM Newsl*. **36**, 25–29, HIRLAM-5 Project, c/o Per Undén, SMHI, S-601 76 Norrköping, SWEDEN.

Makshtas, A. P. 1991. *The Heat Budget of Arctic Ice in the Winter*. Int. Galciol. Soc., Cambridge, England, 77 pp.

Maslanik, J. A., Lynch, A. H., Serreze, M. C. and Wu, W. 2000. A case study of regional climate anomalies in the Arctic: Performance requirements for a coupled model. *J. Climate* **13**, 383–401.

Morcrette, J.-J. 1991. Radiation and cloud radiative properties in the ECMWF forecasting system. *J. Geophys. Res.* **96,** 9121–9132.

Niemelä, S., Räisänen, P. and Savijärvi, H. 2001a. Comparison of surface radiative flux parameterizations. Part I: Longwave radiation. *Atmosph. Res.* **58,** 1–18.

Niemelä, S., Räisänen, P. and Savijärvi, H. 2001b. Comparison of surface radiative flux parameterizations. Part II: Shortwave radiation. *Atmosph. Res.* **58,** 141–154.

Olsson, P. Q. and Harrington, J. Y. 2000. Dynamics and energetics of the cloudy boundary layer in simulations of off-ice flow in the marginal ice zone. *J. Geophys. Res.* **105,** 11889–11899.

Overland, J. E., Spillane, M. C., Percival, D. B., Wang, M. and Mofjeld, H. O. 2004. Seasonal and regional variation of pan-arctic surface air temperature over the instrumental record. *J. Clim.* **17**, 3263–3282.

Pirazzini, R., Vihma, T., Launiainen, J. and Tisler, P. 2002. Validation of HIRLAM boundary-layer structures over the Baltic Sea. *Boreal Env. Res.* **7**, 211–218.

Rodríguez, E., Navascués, B., Ayuso, J. and Järvenoja, S. 2003. Analysis of surface variables and parameterization of surface processes in HIRLAM. Part I: Approach and verification by parallel runs. *HIRLAM Tech. Rep.*, **58**, 41p. + 11p.appendix.

Sass, B. H., Rontu, L. and Räisänen, P. 1994. HIRLAM-2 radiation scheme: Documentation and tests. *Tech. Rep.*, **16**, HIRLAM-3 Project, Available from SMHI, S-60176 Norrköping, Sweden.

Savijärvi, H. 1990. Fast radiation parameterization schemes for mesoscale and short-range forecast models. *J. Appl. Meteorol.* **29**, 437–447.

Savijärvi, H. and Amnell, T. 2001. High resolution flight observations and numerical simulations: Horizontal variability in the wintertime boreal boundary layer. *Theor. Appl. Climatol.* **70**, 245–252.

Savijärvi, H., Arola, A. and Räisänen, P. 1997. Shortwave Optical properties of precipitating waterclouds. *Quart. J. Roy. Meteorol. Soc.* **123,** 883–899.

Savijärvi, H. and Kauhanen, J. 2001. High resolution numerical simulations of temporal and vertical variability in the stable wintertime boreal boundary layer: a case study. *Theor. Appl. Climatol.* **70,** 97–103.

Savijärvi, H. and Matthews, S. 2004. Flow over small heat islands: A numerical sensitivity study. *J. Atmos. Sci.* **61**, 859–868.

Savijärvi, H. and Räisänen, P. 1998. Longwave optical properties of water clouds and rain. *Tellus* **50A**, 1–11.

Sturm, M., Perovich, D. K. and Holmgren, J. 2002. Thermal conductivity and heat transfer through the snow on the ice of the Beaufort Sea. *J. Geophys. Res.* **107**, doi: 10.1029/2000JC000409.

Taylor, P. K. 2002. Air-sea interaction / momentum heat and vapour fluxes. In: *Encyclopedia of Atmospheric Sciences* (Eds Holton, J. P., Curry, J. A. and Pyle, J.). Academic Press, London, 93–102.

Thorpe, A. J. and Guymer, T. H. 1977. The nocturnal jet. *Quart. J. Roy. Meteorol. Soc.* **103**, 633–653.

Tijm, S. 2004. Tuning CBR. *HIRLAM Newsletter* **46**, 18–23, HIRLAM-6 Project, c/o Per Undén, SMHI, S-601 76 Norrköping, SWEDEN.

Undén, P., Rontu, L., Järvinen, H., Lynch, P., Calvo, J. and co-authors. 2002. HIRLAM-5 Scientific Documentation. HIRLAM-5 Project. Norrköping, Sweden, 144 p.

Van Mejgaard, E., Andrae, U. and Rockel, B. 2001. Comparison of model predicted cloud parameters and surface radiation fluxes with observations on the 100 km scale. *Meteor. Atmos. Phys.* **77**, 109–130.

Valkonen, T., Vihma, T. and Doble, M. 2008. Mesoscale modeling of the atmosphere over Antarctic sea ice: A late-autumn case study. *Mon. Wea. Rev.*, in press.

Vihma, T. and Brümmer, B. 2002. Observations and modelling of the on-ice and off-ice air flow over the northern Baltic Sea. *Bound. Lay. Met.* **103**, 1–27.

Vihma, T., Hartmann, J. and Lüpkes, C. 2003. A case study of an on-ice air flow over the Arctic marginal sea ice zone. *Bound. Lay. Met.* **107**, 189–217.

Vihma, T., Lüpkes, C., Hartmann, J. and Savijärvi, H. 2005. Observations and modelling of cold-air advection over Arctic Sea Ice. *Bound. Lay. Met.* **117**, 275–300.

Vihma, T. and Pirazzini, R. 2005. On the factors controlling the snow surface and 2-m air temperatures over the Arctic Sea Ice in winter. *Bound. Lay. Met.* **117**, 73–90.